

Concave Cu-Pd bimetallic nanocrystals: Ligand-based Co-reduction and mechanistic study

Lan Zhang¹, Hongyang Su¹, Mei Sun¹, Youcheng Wang¹, Wenlong Wu¹, Taekyung Yu² (✉), and Jie Zeng¹ (✉)

¹ Hefei National Laboratory for Physical Sciences at the Microscale, Key Laboratory of Strongly-Coupled Quantum Matter Physics of Chinese Academy of Sciences, Center of Advanced Nanocatalysis (CAN-USTC) & Department of Chemical Physics, University of Science and Technology of China, Hefei 230026, China

² Department of Chemical Engineering, College of Engineering, Kyung Hee University, Yongin 446-701, Republic of Korea

Received: 20 December 2014

Revised: 8 February 2015

Accepted: 23 February 2015

© Tsinghua University Press
and Springer-Verlag Berlin
Heidelberg 2015

KEYWORDS

Cu-Pd alloy,
Co-reduction,
concave,
mechanistic study,
hydrogenation of
3-nitrostyrene

ABSTRACT

The synthesis of highly uniform alloy nanocrystals with a concave feature is desirable for applications in catalysis but is an arduous task. This article proposes an initiative protocol for the fabrication of novel Cu-Pd alloy nanocrystals, wherein the volume of decylamine (DA) in the reaction system was found to greatly influence the formation of different morphologies, including the tetrahedron (TH), concave tetrahedron (CTH), rhombohedral-tetrapod (RTP), and tetrapod (TP). The alloy structure of the products arises from the coordination interaction between the DA and metal ions, which affects the reduction potential of Cu and Pd species, and thus yields co-reduction. Other reaction parameters, such as the type of ligand, amount of reductant, and temperature, were also altered to study the growth mechanism, yielding consistent conclusions in the diffusion-controlled regime. As a catalyst, 48-nm Cu-Pd concave tetrahedral nanocrystals were highly active for the hydrogenation of 3-nitrostyrene and exhibited >99.9% chemoselectivity to C=C instead of $-\text{NO}_2$.

1 Introduction

In many cases, bimetallic-alloy nanocrystals not only exhibit a simple combination of the properties related to their two parent metals but can also exhibit great enhancement in a given physicochemical property compared with their monometallic counterparts. This is known as the synergistic effect [1–4]. The enhancement can be attributed to heteroatom bonds, lattice effects, etc., and it introduces a wide range of

applications for alloy nanocrystals [5–9]. In recent years, palladium-based alloy nanocrystals have drawn increasing attention in catalysis owing to their various synergistic effects [10–12]. Pd, which is famous for its high hydrogen solubility, is widely used as an industrial catalyst in petroleum cracking, low-temperature reduction of automobile pollutants, oxidation of CO, etc. [13–16]. The incorporation of a non-noble 3d transition metal, such as Cu, into Pd can not only lower the cost but also achieve a shift of the surface

Address correspondence to Jie Zeng, zengj@ustc.edu.cn; Taekyung Yu, tkyu@khu.ac.kr

d-band center and alter the reaction mechanism [17–20]. Considering its immense potential for catalysis, the controllable synthesis of Cu-Pd alloy nanocrystals is worth investigating.

Two methods are frequently used to synthesize alloy nanocrystals: galvanic replacement and co-reduction [21–30]. Both have been adopted for the synthesis of Cu-Pd alloy nanocrystals [31–34]. Galvanic replacement is typically used for the synthesis of bimetallic hollow nanostructures by adding a secondary metal ion into a solution containing an active metal template. However, alloy structures obtained via galvanic replacement often lack control over the distribution of the two components, leading to a higher ratio of the active metal inside [35]. In contrast, a homogeneous alloy can easily be produced when two kinds of metal salts are reduced simultaneously. It should be noted that Cu^{2+} and Pd^{2+} have very different reduction potentials, making the co-reduction of these two metal ions difficult to achieve. There are only a few cases where co-reduction and shape control are simultaneously realized. For instance, Tan et al. observed that decreasing the concentration of formilide can probe the shape evolution from Cu-Pd nanocubes to irregular polyhedrons and that branched nanocrystals could be formed by increasing the concentration of the precursors [28]. Yu et al. demonstrated a protocol to synthesize Cu-Pd nanocubes by using trioctylphosphine to stabilizing the {100} facets [33]. Thus far, Cu-Pd alloy nanocrystals have mainly been limited to those with a convex surface. Moreover, the growth mechanism of alloy nanocrystals with different structures is seldom elucidated.

Herein, we demonstrate a strategy using decylamine (DA) as a coordinating ligand to achieve controlled co-reduction of the Cu and Pd species. By carefully manipulating the amount of DA and other reaction parameters, such as the temperature and amount of glucose, we prepared Cu-Pd alloy nanocrystals in the shape of a tetrahedron, concave tetrahedron, rhombohedral-tetrapod, and tetrapod. A mechanistic study revealed that the reaction parameters functioned by changing the relative effects of atomic deposition and diffusion [36–38]. Three kinds of as-prepared Cu-Pd bimetallic nanocrystals—48-nm concave tetrahedrons, 50-nm rhombohedron-tetrapods, and 10-nm

concave tetrahedrons—were employed as catalysts for the hydrogenation of 3-nitrostyrene. Among the examined catalysts, the 48-nm Cu-Pd concave tetrahedrons were found to have the highest catalytic activity toward the hydrogenation of 3-nitrostyrene and could afford >99.9% chemoselectivity toward the production of 3-nitroethylbenzene.

2 Experimental section

2.1 Chemicals and materials

Sodium tetrachloropalladate(II) (Na_2PdCl_4), decylamine (DA), trioctylamine (TOA), ethylenediamine (EDA), activated carbon (C), and 3-nitrostyrene ($\text{C}_8\text{H}_7\text{NO}_2$) were purchased from Sigma-Aldrich. Copper(II) chloride dehydrate ($\text{CuCl}_2 \cdot 2\text{H}_2\text{O}$), poly(vinyl pyrrolidone) (PVP, $M_w \approx 40,000$), glucose (α or β form), N,N-dimethylformamide (DMF), sodium hydroxide (NaOH), hydrochloric acid (HCl), dodecane ($\text{C}_{12}\text{H}_{26}$), and ethanol ($\text{C}_2\text{H}_5\text{OH}$) were purchased from Sinopharm Chemical Reagent Co. Ltd. (Shanghai, China). All chemicals were used as received, without further purification. Deionized (DI) water with a resistivity of 18.2 M Ω -cm was used for the preparation of all aqueous solutions.

2.2 Synthesis of Cu-Pd bimetallic nanocrystals with controlled structures

For the synthesis of Cu-Pd concave tetrahedrons, 9.0 mg of Na_2PdCl_4 , 5.2 mg of $\text{CuCl}_2 \cdot 2\text{H}_2\text{O}$, 300 mg of PVP, 80 μL of DA, and 250 mg of glucose were dissolved in 5 mL of DMF in a 20-mL vial. After being capped, the vial was transferred into an oil bath and heated at 110 °C under vigorous magnetic stirring for 2 h. The obtained Cu-Pd nanocrystals were collected by centrifugation and washed several times with DI water and ethanol to remove the excess PVP, DA, and glucose.

For the synthesis of Cu-Pd alloy nanocrystals with different structures, we used the same procedure as described for the 48-nm concave tetrahedrons, changing only the volume of DA and the reaction temperature. The detailed experimental conditions for each synthesis are presented in Table 1.



Table 1 Reaction Conditions for Synthesis of Cu-Pd Bimetallic Nanocrystals and Structural Information of Resulting Cu-Pd Nanocrystals with Different Morphologies

T/ °C	V _{DA} ^a / μL	Shape ^b	Size / nm	Composit-i on ^c / %		Results /Figure
				Cu	Pd	
70	80	TH	7 ± 1	10	90	S16A
80	65	TH	9 ± 1	10	90	6A
80	80	CTH	10 ± 1	11	89	6B
80	95	RTP	10 ± 1	12	88	6C
80	150	TP	30 ± 1	15	85	6D
95	80	CTH	35 ± 1	9	91	S16B
110	65	TH	20 ± 1	3	97	1A
110	80	CTH	48 ± 2	5	95	1B, 2
110	95	RTP	50 ± 2	7	93	1C, 3
110	150	TP	70 ± 5	16	84	1D
120	80	S	8 ± 2	4	96	S16C

^a V_{DA} = volume of DA.^b TH = tetrahedron, CTH = concave tetrahedron, RTP = rhombohedron-tetrapod, TP = tetrapod, S = sphere.^c The atomic ratios of Cu and Pd were investigated by ICP-AES.

2.3 Hydrogenation of 3-nitrostyrene

First, 2.7 mg of activated carbon was added to an ethanol solution containing 0.3 mg of 48-nm Cu-Pd concave tetrahedrons (Cu-Pd-1). After stirring for 2 h at room temperature, the mixture was dried in vacuo, yielding 10% Cu-Pd-1/C. The preparation of the other two catalysts followed the same procedure as that of the 10% Cu-Pd-1/C.

The procedure for the hydrogenation of 3-nitrostyrene by the three different types of Cu-Pd nanocrystals or commercial Pd/C catalysts was as follows: 3 mg of the catalysts was placed in a three-necked round-bottom flask, followed by the addition of dodecane (3 mL) and 3-nitrostyrene (0.3 mmol). The flask was fitted with a gas inlet tube and a condenser with a liquid seal at the end. A stream of H₂ was conducted into the reaction mixture at a constant flow rate (1–2 bubbles/min). The reaction was performed at 75 °C in an oil bath with magnetic stirring at 300 rpm. After the completion of the reaction, the catalysts were removed by centrifugation, and the supernatant was analyzed by GC-MS to determine the conversion and selectivity.

2.4 Instrumentation

Transmission electron microscopy (TEM) images were taken using a Hitachi H-7650 transmission electron microscope at an acceleration voltage of 100 kV. High-resolution TEM (HRTEM), high-angle annular dark-field scanning TEM (HAADF-STEM), and energy dispersive X-ray (EDX) analysis were performed with a JEOL ARM-200F field-emission transmission electron microscope operating at an accelerating voltage of 200 kV using Mo-based TEM grids. X-ray diffraction (XRD) characterization was performed using a Philips X'Pert Pro X-ray diffractometer with a monochromatized Cu Kα radiation source and a wavelength of 0.1542 nm. The atomic ratio of Cu and Pd was investigated by inductively coupled plasma atomic emission spectrometry (ICP-AES, Atomscan Advantage, Thermo Jarrell Ash, USA). To obtain further evidence for the composition of the products, X-ray photoelectron spectra (XPS) were used. These were recorded on an ESCALAB-250 spectrometer having a monochromatic Al Kα X-ray source (hν = 1486.6 eV), with a spot size of 500 μm. The extinction spectra were obtained using a Cary 60 UV–vis spectrophotometer. Fourier transform infrared (FT-IR) spectra were measured using a Bruker Vector-22 FT-IR spectrometer from 400 to 4,000 cm⁻¹ at room temperature. All gas chromatography-mass spectrometry (GC-MS) experiments were performed and recorded by a GC-MS (Agilent Technologies, GC 7890A, MS 5975C).

3 Results and discussion

3.1 Coordination effect of DA

The standard reduction potential of the PdCl₄²⁻/Pd pair (0.62 V) is more positive than that of the Cu²⁺/Cu pair (0.34 V) [39], which indicates that PdCl₄²⁻ can be reduced far more easily than Cu²⁺. It is reported that under-potential deposition (UPD) and galvanic replacement reaction (GRR) usually occur between two metal precursors with greatly different reduction potentials, such as Cu²⁺ and Pd²⁺. One feasible method for avoiding the separate nucleation of the two metals is to introduce a coordination ligand having a far stronger coordination interaction with Pd²⁺ than

with Cu^{2+} . Such ligands can make the reduction potentials of Cu^{2+}/Cu and Pd^{2+}/Pd become close, leading the two species to reduce simultaneously and thereby restraining the occurrence of UPD and GRR. Furthermore, a stronger coordination with Pd^{2+} could lower the concentration of Pd^{2+} (c_A). According to classic chemical kinetics ($v_A = kc_A^n$), a lower concentration of Pd^{2+} reduces the reduction rate far more than the case of Cu^{2+} , balancing the reduction rates of the two species. The close reduction rates further promote the co-reduction process. Considering these two aspects, the selection of an appropriate coordination ligand is an efficient route to synthesize Cu-Pd alloy nanocrystals. It is reported that the reduction potentials of $\text{Pd}(\text{NH}_3)_4^{2+}/\text{Pd}$ pair (0 V) [40] and $\text{Cu}(\text{NH}_3)_4^{2+}/\text{Cu}$ pair (0 V) [39] are equal. Thus, the amine may be an efficient additive for the co-reduction strategy for Pd and Cu species. In this case, we chose DA as the coordination ligand.

To validate the existence of coordination, UV-vis and FT-IR measurements were performed. Figure S1 shows the UV-vis extinction spectra of different coordination complexes with a corresponding photograph of the samples. These complexes were all dispersed in DMF, and the molar ratio of metal ions to DA remained the same. The extinction peaks of pure CuCl_2 and pure Na_2PdCl_4 were located at 437 and 442 nm, respectively. When DA was involved in the system, the extinction peaks shifted to 713 and 336 nm, respectively, which agreed with the visual observation of the change in the color of the solution. In addition, FT-IR spectra (Fig. S2) were used to characterize DA, the Pd^{2+} -DA complex, and the Cu^{2+} -DA complex. The absorption peaks of DA around 3,330 and $1,650\text{ cm}^{-1}$ were attributed to N-H stretching vibration and N-H in-plane bending vibration, respectively. When DA was mixed with Na_2PdCl_4 or CuCl_2 , these two peaks shifted; the difference was more obvious in the case of Na_2PdCl_4 . This observation is ascribed to the changes in the N-H vibration modes caused by the coordination interaction between the amine and Cu^{2+} or Pd^{2+} . It can thus be concluded that both the Cu^{2+} and Pd^{2+} have coordination interactions with DA in the solution.

3.2 Structural analysis of Cu-Pd bimetallic nanocrystals with controlled structures

To fabricate a homogenous Cu-Pd alloy, DA was used as a coordination ligand to balance the reducing rate of Cu and Pd species in DMF [25, 26]. In a typical synthesis, precursors—including Na_2PdCl_4 and $\text{CuCl}_2 \cdot 2\text{H}_2\text{O}$ —PVP as dispersing agent, DA as the coordination ligand, and glucose as the reducing agent, were dissolved in DMF to form a homogeneous mixture. The reaction was conducted by heating the mixture in an oil bath at 110°C for 2 h while stirring. By varying the volume of DA (see Table 1 for details), Cu-Pd nanocrystals with different structures were prepared, whose representative TEM images are shown in Fig. 1. When $65\text{ }\mu\text{L}$ of DA was added to the reaction system, conventional tetrahedrons (THs) enclosed by a flat surface with a size of $20 \pm 1\text{ nm}$ were obtained, as shown in Fig. 1(a). With the addition of $80\text{ }\mu\text{L}$ of DA, it was obvious that each side face of the tetrahedron was excavated at the center, forming concave tetrahedrons (CTHs) with a typical yield of $>90\%$ (Fig. 1(b)). These concave nanocrystals had a uniform edge length of $48 \pm 2\text{ nm}$. As the volume of DA was increased to $95\text{ }\mu\text{L}$, the growth of nanocrystals tended to occur on the corners of tetrahedrons, yielding high-purity tetrapods with an edge length of $50 \pm 2\text{ nm}$, as shown in Fig. 1(c). The as-obtained tetrapods, resembling four rhombohedron-like arms ($\sim 20\text{ nm}$ in length) jointed together by one shared tetrahedron at the center, were called rhombohedral tetrapods (RTPs). Further increasing the volume of DA to $150\text{ }\mu\text{L}$ led to an overgrowth on each arm, yielding tetrapods (TPs) enlarged to $70 \pm 5\text{ nm}$ in size (Fig. 1(d)). Similar to the model proposed in the inset of Fig. 1(d), in the RTPs, each arm of the TPs comprises two rhombohedrons jointed together.

A representative TEM image of the as-prepared CTH is shown in Fig. 2(a). It is clear that each CTH is curved inward, with a trigonal pyramid on each side face (Fig. 2(b)). As shown in Fig. S3(a), SEM images indicated that the CTHs with an edge length of $\sim 48\text{ nm}$ had a high purity. The selected-area electron diffraction (SAED) measurement on an individual CTH indicated its single-crystalline nature, as shown

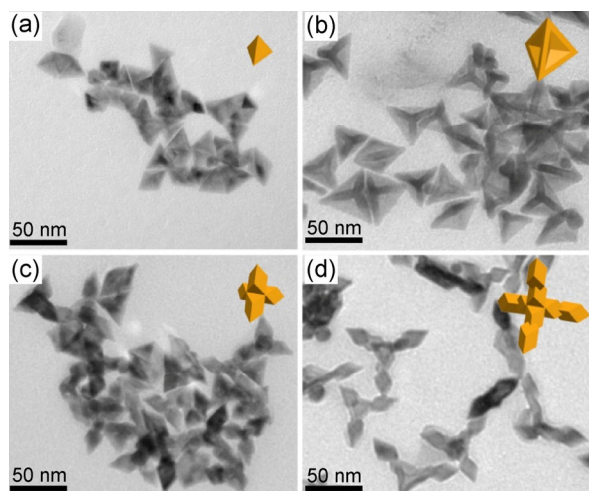


Figure 1 TEM images of Cu-Pd bimetallic nanocrystals obtained at 110 °C in the presence of (a) 65, (b) 80, (c) 95, and (d) 150 μL of DA. All other reaction conditions are the same: Na_2PdCl_4 (9.0 mg, 6.1 mM), $\text{CuCl}_2 \cdot 2\text{H}_2\text{O}$ (5.2 mg, 6.1 mM), PVP (300 mg), glucose (250 mg), DMF (5 mL), reaction temperature (110 °C), reaction time (2 h). Inset shows corresponding three-dimensional geometric model for each type of structure.

in Fig. 2(c). Figure 2(d) shows the HRTEM image recorded along the $[111]$ zone axis of the regions marked by boxes in Fig. 2(a). The measured lattice spacings (1.4 \AA) marked in Fig. 2(d) can be indexed to $\{220\}$ planes. As shown in the enlarged HRTEM image on the edge, the fringes with an interplanar spacing of 1.4 \AA were running along the edge of tetrahedron (Fig. S4). Considering the model analysis, we confirm that the concave side facing toward the center of the tetrahedron were essentially $\{110\}$ facets [38, 47]. Together with the TEM image and SAED pattern, the HAADF-STEM image (Fig. 2(e)) illustrates good geometric agreement between the CTH morphology and the model shown in Fig. 2(b), on which STEM-EDX mapping was induced. Figures 2(f) and 2(g) show the elemental distributions of Cu and Pd, respectively. The full coverage of both Cu and Pd confirms the alloy structure. The merged image (Fig. 2(h)) further reveals overlapping of both Cu and

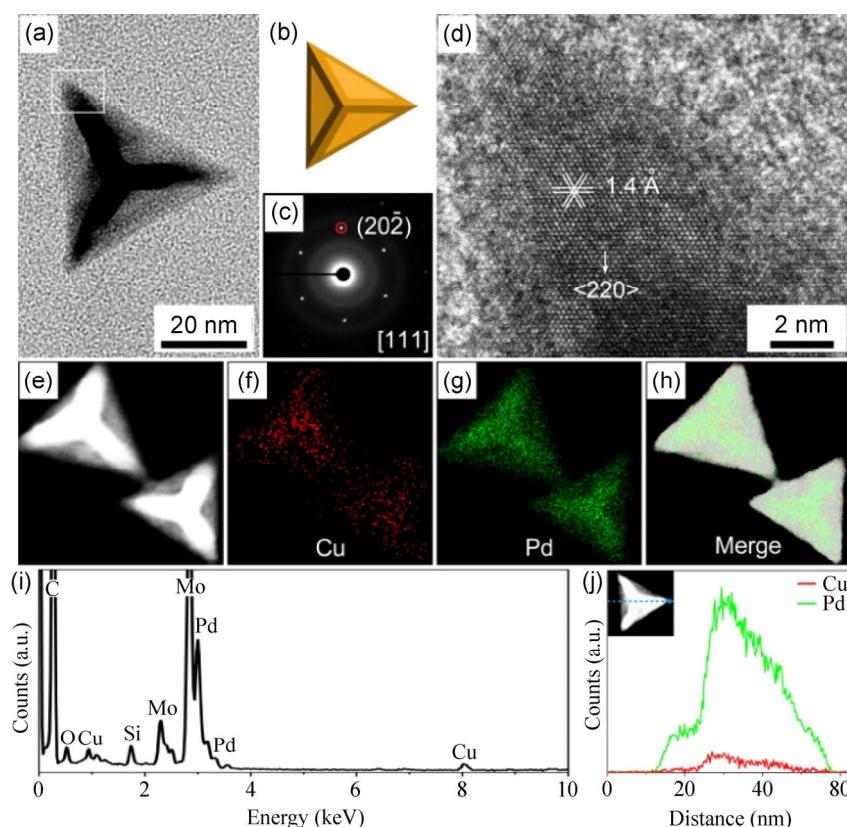


Figure 2 Structure and composition characterizations of concave Cu-Pd tetrahedrons shown in Fig. 1(b). (a) TEM image of the as-prepared CTH. (b) Ideal structure model of nanocrystal. (c) Corresponding SAED pattern with electron beam directed along $[111]$ zone axis. (d) HRTEM image taken from region marked by box in (a). (e) HAADF-STEM image of two individual nanocrystals. (f, g) STEM-EDX mapping image for Cu (f) and Pd (g). (h) Merged image of (e), (f), and (g). (i) EDX spectrum of two nanocrystals. (j) Line-scanning profiles recorded from single Cu-Pd concave tetrahedron along symmetric axis.

Pd throughout the nanocrystals. The corresponding EDX spectrum of the CTHs (Fig. 2(i)) suggests that the atomic ratio of Cu was 5%, which was consistent with the ICP-AES analysis (shown in Table 1). The EDX line-scanning profile recorded from a single Cu-Pd concave tetrahedron along the symmetric axis further supports the homogeneous distribution of the two metal components, as shown in Fig. 2(j).

The structure and composition characterizations of the Cu-Pd RTPs are shown in Fig. 3. It can be seen from the TEM image of a typical RTP nanocrystal (Fig. 3(a)) that the tetrapod was 50 nm in size and had an arm length of 20 nm. Figure S3(b) shows its shape homogeneity. A geometric model viewed from the same direction for the case of CTHs (along [111] zone axis) is illustrated in Fig. 3(b), suggesting that a

typical RTP is completely covered by {111} facets, with 12 rhombus-like faces and 12 regular triangular faces included. The SAED pattern (Fig. 3(c)) recorded from the same RTP indicates a single-crystalline structure. In Fig. 3(d), the HRTEM image of the RTP shows lattice fringes with an interplanar spacing of 1.4 Å, corresponding to the {220} planes. STEM-EDX mapping was induced on an individual RTP as shown in Fig. 3(e), confirming the alloy structure of the Cu-Pd RTPs (Figs. 3(f)–3(h)). The corresponding EDX spectrum (Fig. 3(i)) indicates that the atomic ratio of Cu was 10%, which is fairly close to that (7%) measured by ICP-AES (Table 1). EDX line-scanning analysis along the symmetric axis of a single Cu-Pd RTP further confirmed its alloy structure (Fig. 3(j)).

XRD analysis was used to reveal the crystalline

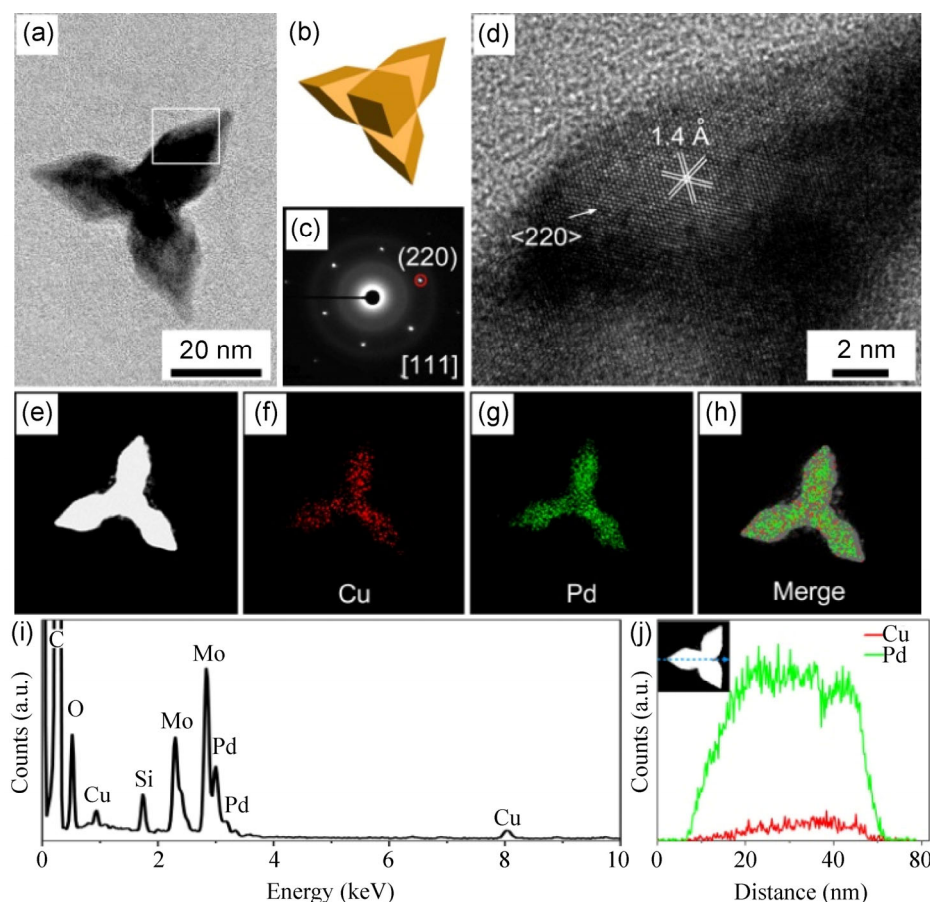


Figure 3 Structure and composition characterizations of Cu-Pd RTPs shown in Fig. 1(c). (a) TEM image of typical RTP nanocrystal. (b) Ideal structure model of nanocrystal. (c) Corresponding SAED pattern. (d) HRTEM image taken from region marked by box in (a). (e) HAADF-STEM image of individual RTP nanocrystal. (f, g) STEM-EDX mapping image for Cu (f) and Pd (g). (h) Merged image of (e), (f), and (g). (i) EDX spectrum of individual nanocrystal. (j) Line-scanning profiles recorded from single Cu-Pd RTP along symmetric axis. In proposed model, four rhombohedrons are jointed together by one shared tetrahedron at the center to form the tetrapod. Each rhombohedron was enclosed by six rhombus-like {111} faces.



structure of the Cu-Pd alloy CTHs and RTPs. As shown in Fig. S5(a), small biases in the peak position can be observed between the as-prepared nanocrystals and pure face-centered cubic (*fcc*) Pd (JCPDS no. 46-1043) because the contents of Cu in the products were fairly low, and the peak positions of *fcc* Cu (JCPDF: 85-1326) and *fcc* Pd (JCPDF: 46-1043) were close. After partly enlarging the XRD pattern, we clearly observed that each peak occurred amongst that of pure *fcc* Cu and pure *fcc* Pd, suggesting the possibility of an alloy structure (Fig. S5(b)–5(d)). According to the hypothesis of the alloy structure, the atomic ratios of Cu were calculated to be 4% and 9% for the Cu-Pd alloy CTHs and RTPs, respectively, using Vegard's law. [41] This result accords with those obtained by ICP-AES and EDX measurements.

To analyze the composition on the surface of the novel structures shown in Fig. 1, XPS measurements were conducted for each of the four nanocrystals [42]. The atomic ratio of Cu can be determined by integrating the area under the high-resolution peaks (Fig. S6). The XPS data show that the ratio of Cu on the surface of the samples was almost equal to that in the bulk nanocrystals measured by ICP-AES, corroborating the co-reduction of Cu^{2+} and Pd^{2+} (Fig. S7). To prove that DA plays a vital role in this co-reduction strategy, we conducted an experiment using the typical synthesis, except for the addition of a tertiary amine (in this case, TOA). The UV-vis extinction spectrum taken from the DMF solution containing Na_2PdCl_4 and TOA shows that the peak was located at 445 nm, which was nearly the same as that for pure Na_2PdCl_4 (Fig. S8). However, as for the solution containing CuCl_2 and TOA, a weak extinction peak was recorded at 437 nm, and another broad peak appeared at 830 nm. This indicates the existence of both free Cu^{2+} ions and a Cu^{2+} -TOA complex. It is obvious that TOA has weaker coordination interactions with metal ions compared with DA, which is probably because of its steric effect [43]. Although Cu^{2+} can coordinate with TOA, PdCl_4^{2-} cannot achieve ligand exchange with TOA, owing to the weak coordination ability, which leads to an increased difference in reduction potential between Cu and Pd species. Figure S9 shows the TEM image of Cu-Pd nanocrystals prepared in the experiments with the addition of TOA. Most of the products were

small (~10 nm) sphere-like nanocrystals. The ICP-AES analysis reveals that the content of Pd exceeds 97% in the nanocrystals. When neither DA nor TOA was added into the reaction system, a similar result was obtained: thermodynamically favored polyhedrons with a high ratio of Pd (>97%) were acquired (Fig. S10). We thus conclude that the coordination interaction was fairly critical to the co-reduction and the formation of alloy nanocrystals.

As previously mentioned, the reduction potentials of Cu and Pd were quite different. We bring the reduction rates of the two precursors close to each other with the addition of DA. However, the atomic ratio of Cu was still far lower than that of Pd in the products. There are two approaches to manipulate the composition ratio: 1) varying the volume of DA to manipulate the coordination degree and 2) adjusting the molar ratio of the metal precursors. Unfortunately, both approaches affect the reaction kinetics and thus the final shape of products. It remains a challenge to manipulate the composition ratio while maintaining the shape of the product in this reaction system.

According to the aforementioned results, non-uniform polyhedrons with a large size were prepared when no DA was involved in the reaction system. The large size of the product was probably due to the lack of confinement, which was caused by the absence of a capping agent [44]. In addition, a morphological analysis of the nanocrystals synthesized in the presence of DA and TOA indicates that the amine (both DA and TOA) could function as a capping agent. Specifically, DA would preferentially adsorb on {111} facets (side faces of tetrahedrons), which is essential for the formation of the tetrahedral structure [38]. Additionally, TOA could control the size via the capping effect without the selection of a specific facet. This is probably because DA is a kind of primary amine with only one carbon chain linked to the N atom. When the N atoms adsorb on the surfaces of the as-prepared nanocrystals, the long carbon chains tend to form ordered assembled structures because of the van der Waals force [45]. However, TOA, as a tertiary amine, has a strong steric effect that hinders the assembly. To further explore the capping effect of the primary amine, a bidentate primary amine (in this case, EDA) was introduced as a substitute for DA. The obtained product exhibited a

high contrast and angular corners under TEM, likely owing to the overlapping of multiple concave tetrahedrons (Fig. S11). Given that one EDA molecule adsorbs on two concave tetrahedrons simultaneously, the concave tetrahedrons are assembled together as a result. Therefore, these findings are strong evidence that the amino group could cap on the {111} facets and help maintain the tetrahedral structure.

3.3 Effect of amine on acceleration of reaction

From the viewpoint of the coordination effect, the presence of DA should inhibit the growth of Cu-Pd nanocrystals. Interestingly, in the absence of amine, the reaction solution remained clear and transparent, and no obvious product was obtained at 2 h. The final product shown in Fig. S10 was generated at 12 h. In contrast, the solution color quickly turned dark at ~5 min in the presence of DA, and similar phenomena were observed in the cases of TOA and EDA. In the present work, the reaction seems to be accelerated by the addition of amine. To better understand how the reaction kinetics were related to the volume of DA, we conducted a set of time-dependent experiments for the four types of nanocrystals shown in Fig. 1 and collected the samples obtained at different times. After the samples were dissolved with aqua regia, ICP-AES was used to monitor the process of these reactions. As shown in Fig. 4(a), for the synthesis of THs with 65 μL of DA, the concentration of reduced metal atoms ($[\text{Cu}^0] + [\text{Pd}^0]$) in the sample increased only to $0.77 \mu\text{mol}\cdot\text{mL}^{-1}$ at 5 min. However, the concentrations of reduced metal atoms quickly increased to 1.38, 1.49, and $3.11 \mu\text{mol}\cdot\text{mL}^{-1}$ at 5 min with 80, 95, and $150 \mu\text{L}$ of DA involved, respectively. These results clearly reveal that increasing the volume of DA resulted in the acceleration of the reduction. Meanwhile, the atomic ratio of Cu in the four products increased with the reaction time (Fig. 4(b)). For each type of nanocrystal, the atomic content of Cu remained almost constant during the reaction. It was also observed that the atomic ratio of Cu increased with the volume of DA in the system, indicating that the reduction rates of Cu^{2+} and Pd^{2+} became close with the addition of a larger volume of DA, owing to the more obvious co-reduction.

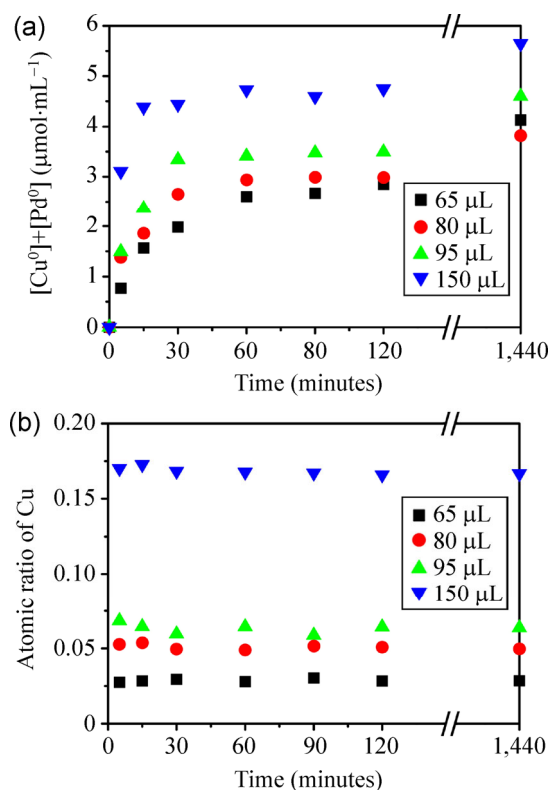


Figure 4 (a) ICP-AES kinetic data for reactions containing 65, 80, 95, and $150 \mu\text{L}$ of DA. (b) Plots showing atomic ratio of Cu in the four products as a function of reaction time.

Clearly, the reaction can be accelerated by DA. This is probably because of the enhancement in alkalinity caused by introducing a Lewis base (in this case, DA). It is well acknowledged that the alkaline environment can enhance the reduction power of the aldehyde group in glucose (reducing agent) by consuming its oxidation product (gluconic acid) and can thus promote the reduction rate [46, 47]. To test this hypothesis, we manipulated the acid-alkaline environment of the standard reaction condition for Cu-Pd CTHs by adding HCl or NaOH. Figure S12 shows the corresponding TEM images of the products achieved in the presence of HCl and NaOH, respectively. We observe that the dominant products were tetrahedrons and slightly concave tetrahedrons when HCl was involved in the system, similarly to the case with less DA. With the addition of NaOH, RTPs and TPs were prepared, which was consistent with the products obtained when more DA was used. These results confirm that the alkalinity of the amine can promote the reduction reaction, leading to the preferential formation of different morphologies.

3.4 Effect of Cu ions

To explore the role of Cu ions in the shape evolution of the nanocrystals, we conducted experiments using the standard procedure for 48-nm CTHs, except with varying amounts of CuCl_2 (Fig. S13). When no CuCl_2 was added, nanocrystals without certain facets were obtained, most of which exhibited twinning structures (Fig. S13(a)). When 0.2 mg of CuCl_2 (1/30 of $[\text{Na}_2\text{PdCl}_4]$) was added, tetrahedrons started to appear (Fig. S13(b)). As shown in Figs. S13(c)–13(e), it can be concluded that the purity of the obtained CTHs can be improved with the addition of more CuCl_2 in a certain range. However, when the concentration of CuCl_2 was five times that of Na_2PdCl_4 , the rate of overgrowth on the edge started to slow down (Fig. S13(f)). Clearly, Cu ions play an important role in the structural evolution of nanocrystals, although the atomic ratio of Cu in the final product is low. We suspect that Cu ions affect the nucleation, favoring the generation of single-crystal seeds. Thus, the addition of CuCl_2 unifies the morphology. However, excessive amounts of CuCl_2 affect the reaction kinetics and thus the final shape of the products.

3.5 Effect of reducing agent

Changing the concentration of the reducing agent, glucose, may be the most direct way to control the reaction kinetics and thus the structure of the products. To establish a relationship between the reaction kinetics and morphological change, we conducted an experiment to vary the amount of glucose added to the system. When the amount of glucose was reduced to 25 mg (1/10 of amount used in typical synthesis), CTHs and octahedrons 25 nm in size were obtained (Fig. 5(a)). As the amount of glucose was increased to 750 mg (thrice the standard amount), most of the products were RTPs (Fig. 5(b)). These results indicate that increasing the amount of glucose promotes protrusion. This process probably occurred because of the preferential growth at corner sites caused by the acceleration of the reaction, which is consistent with the phenomenon observed when increasing the volume of DA.

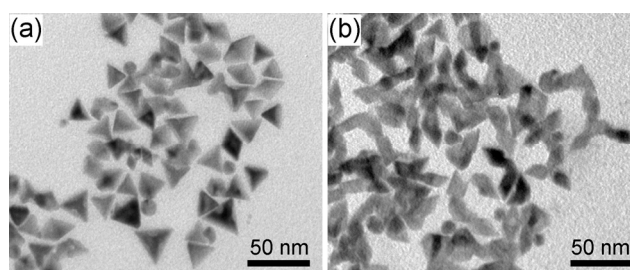


Figure 5 TEM images of products obtained using standard procedure, except varying amount of glucose used: (a) 25 and (b) 750 mg. Amount of glucose used in standard condition was 250 mg.

3.7 Effect of PVP

The role of PVP should be clarified in order to elucidate the formation mechanism of Cu-Pd bimetallic nanocrystals with different structures. The products obtained using the standard procedure, except for the absence of PVP, are shown in Fig. S14. Here, most of the nanocrystals aggregated together owing to the loss of the dispersion effect of the PVP. [49] Furthermore, the size distribution of the product was extensive, and polyhedral nanocrystals were produced during the inhomogeneous synthesis. Thus, in this case, the major function of the PVP is to prevent the as-prepared nanocrystals from aggregating, and it is not effective to alter the morphology.

3.8 Effect of reaction temperature

We performed a set of experiments using the standard procedure but at 80 °C (see Table 1 for details). Figs. 6(a)–6(d) show representative TEM images of the nanocrystals obtained in the presence of 65, 80, 95, and 150 μL of DA, respectively. In parallel with Figs. 1(a)–1(d), by controlling the volume of DA in the system, conventional THs (9 ± 1 nm in size, Fig. 6(a)), CTHs (10 ± 1 nm in size, Fig. 6(b)), RTPs (10 ± 1 nm in size, Fig. 6(c)), and TPs (30 ± 1 nm in size, Fig. 6(d)) were successfully synthesized, but with smaller sizes. Higher-magnification TEM images of the Cu-Pd RTPs and TPs are presented in Fig. S15. Each arm of the RTPs consists of a rhombohedron, while each arm of the TPs consists of two that form a longer zigzag arm. The shape evolution and volume of DA follow similar trends as those at 110 °C. The EDX spectrum (Fig. S16)

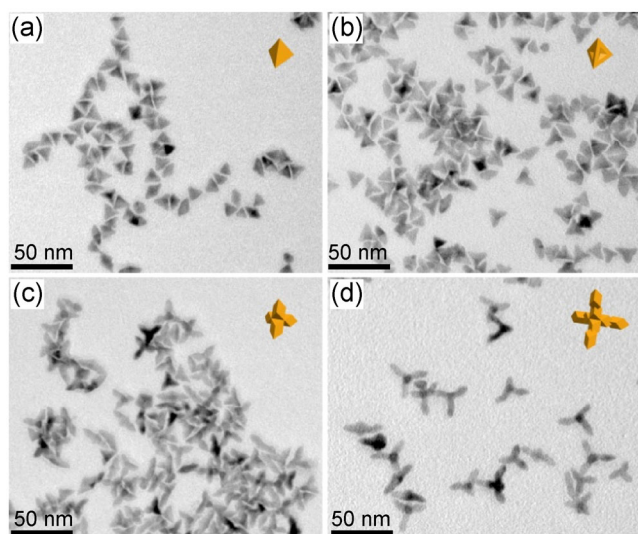


Figure 6 TEM images of Cu-Pd alloy nanocrystals synthesized at 80 °C in the presence of (a) 65, (b) 80, (c) 95, and (d) 150 μL of DA. All other reaction conditions are the same: Na_2PdCl_4 (9.0 mg, 6.1 mM), $\text{CuCl}_2 \cdot 2\text{H}_2\text{O}$ (5.2 mg, 6.1 mM), PVP (300 mg), glucose (250 mg), DMF (5 mL), reaction time (2 h). Inset shows corresponding three-dimensional geometric model for each type of structure.

reveals that the atomic ratio of Cu was $\sim 15\%$, which agrees with the atomic ratio measured by ICP-AES (11%). This is probably because the stability of the complex is enhanced as the reaction temperature is lowered [48]. This enhancement leads to the reduction rates of the two species being close, yielding Cu-rich nanocrystals.

When the reaction was performed at 70 °C, only small tetrahedrons with no concave surfaces and a size of approximately 7 nm were obtained (Fig. S17(a)). At 95 °C, the concave feature became obvious, and most of the products were concave tetrahedrons with an enlarged size of 35 ± 1 nm (Fig. S17(b)). As the temperature was increased to 120 °C, sphere-like nanocrystals were observed, attributed to the change of the nucleation mechanism (Fig. S17(c)). It seems that morphological evolution was not obvious when the reaction temperature was changed. This is probably because variation in the reaction temperature changes the reduction rate and diffusion rate simultaneously.

3.9 Formation mechanism of Cu-Pd bimetallic nanocrystals with different structures

As previously mentioned, the effects of the amine are

critical to the formation of different Cu-Pd alloy nanocrystals. Essentially, DA in the solution will coordinate with Pd^{2+} and Cu^{2+} ions, leading to the co-reduction of Cu^{2+} and Pd^{2+} . In principle, the addition of DA decreases the ability of metal ions to be reduced by glucose. However, our observations indicate that the reaction can be accelerated by increasing the volume of DA. This is probably because increasing the volume of DA makes the reaction environment more alkaline and thus enhances the reduction power of glucose. Furthermore, DA can serve as a capping agent, selectively binding to the {111} facets. This promotes the corner-selected deposition of atoms by slowing down the deposition rate on the side faces, which is essential to dictate the formation of the tetrahedral structure.

Considering the results from the previous experiments, we conclude that a fast reduction rate promotes selective growth at the corner sites. Accordingly, a plausible mechanism for the formation of different types of Cu-Pd bimetallic nanocrystals is proposed (Fig. 7). In a general growth process, the newly reduced Cu and Pd atoms tend to deposit at the corner sites of tetrahedral seeds (Fig. 7(a), 1) owing to the blocking effect of DA as the capping agent on {111} facets. The rate of this effect is called V_1 . The adatoms may not remain at the same sites where the depositions occurred; rather, they can migrate to other sites, including edges (Fig. 7(a), 2) and side surfaces (Fig. 7(a), 3), via surface diffusion. The diffusion rates from corners to edges and from corners/edges to side faces are called V_2 and V_3 , respectively. Different growth modes (Fig. 1) can result from the relative effects of the deposition and diffusion processes (Fig. 7(b)). When the volume of DA was relatively small (65 μL), the growth mode was mostly diffusion-controlled ($V_1 \approx V_2 \approx V_3$). The adatoms had enough time to migrate to other sites, and therefore, the shape of tetrahedron was maintained (Fig. 1(a)). As the volume of DA was increased to 80 μL , the side faces were strongly capped by DA, and thus, the probability of the atoms migrating from the corner sites to the side faces was low, and overgrowth mainly occurred on the edges. In the case of $V_1 \approx V_2 > V_3$, the atoms could only diffuse to the edges, leading to the formation of concave tetrahedral nanocrystals with each side face excavated by a



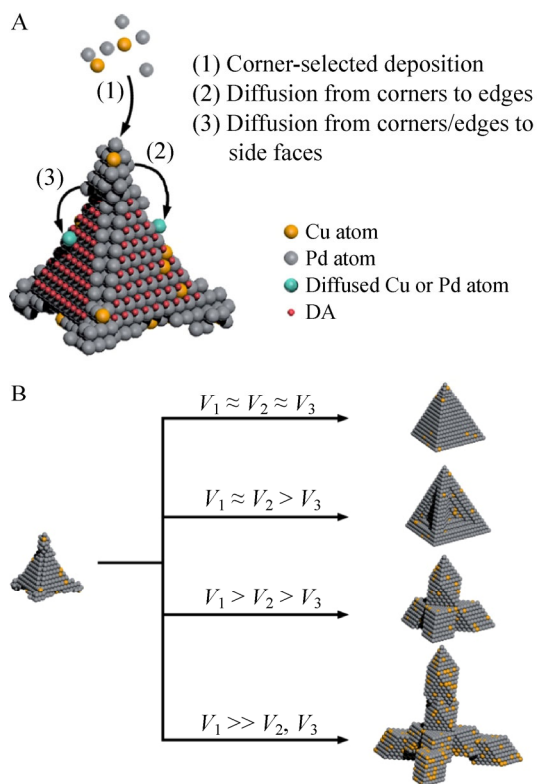


Figure 7 Schematic illustrating plausible mechanism for formation of Cu-Pd alloy nanocrystals.

trigonal pyramid (Fig. 1(b)). As mentioned beforehand, increasing the volume of DA increases the deposition rate (V_1), leading to the case of $V_1 > V_2 > V_3$. Consequently, the overgrowth that mainly occurred at the corner sites makes it possible to form the structure of the RTP (Fig. 1(c)). Further increasing the volume of DA to 150 μL leads to an even higher V_1 and probably $V_1 \gg V_2, V_3$. In this case, another rhombohedron was allowed to grow on each arm of the RTP, and nanocrystals with the shape of TP were obtained (Fig. 1(d)).

To validate the proposed mechanism, additional time-dependent experiments were conducted. As shown in Fig. S18, the intermediate nanocrystals produced at different times were characterized by TEM. Figures S18(a)–18(c) detail the morphological evolution of Cu-Pd THs during the synthesis. These Cu-Pd polyhedrons obtained at $t = 5$ min had an edge length of ~ 10 nm (Fig. S18(a)). As the growth continued, their average edge length increased to ~ 11 nm at 15 min (Fig. S18(b)), ~ 14 nm at 30 min (Fig. S14(c)), and ~ 20 nm at 2 h (Fig. 1(a)). In the case of the CTHs, THs with an

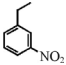
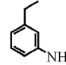
edge length of ~ 12 nm were produced in the initial stage ($t = 5$ min, Fig. S18(d)). After the reaction proceeded for 15 min, overgrowth started to occur on the edges (Fig. S18(e)). At 30 min, the edge length of the products had increased to 30 nm, and the cavity was more obvious (Fig. S18(f)). Similarly, in the case of the RTPs, small THs were obtained in the initial stage ($t = 5$ min, Fig. S18(g)). At 15 min, overgrowth mainly occurred at the corner sites owing to the increase of the deposition rate, resulting in the appearance of RTPs with an arm length of ~ 10 nm (Fig. S18(h)). Typical RTPs formed when the reaction was prolonged to 30 min (Fig. S18(i)). The TP were obtained under a higher deposition rate. Even at 5 min, some small tetrapods had formed (Fig. S18(j)). Further growth and second-generation overgrowth are displayed in the products collected at 15 min (Fig. S18(k)) and 30 min (Fig. S18(l)), respectively.

3.10 Catalytic behaviors of Cu-Pd bimetallic nanocrystals

The unique concave structure and characteristics of the Cu-Pd nanocrystals motivated us to investigate their catalytic properties [50–56]. The catalytic activity and selectivity of the two typical Cu-Pd nanocrystals shown in Figs. 1(b) and 1(c) were evaluated for the hydrogenation of 3-nitrostyrene using H_2 (1 atm, 75°C , under magnetic stirring at 300 rpm). Table 2 clearly indicates that when the reduction reaction proceeded for 0.5 h, the conversions of 3-nitrostyrene related to different catalysts were 77.7% (Cu-Pd-1, 48-nm CTHs) and 35.9% (Cu-Pd-2, 50-nm RTPs), respectively. The corresponding turnover frequency (TOF) values were $1,205.4\text{ h}^{-1}$ (Cu-Pd-1) and 843.9 h^{-1} (Cu-Pd-2), illustrating the significantly higher activity of the concave tetrahedral structure compared with the tetrapod structure. According to the discussion, we also applied smaller Cu-Pd concave tetrahedrons (Fig. 6(b)) to the catalytic reaction. It is acknowledged that smaller catalysts often exhibit higher catalytic activity because of their relatively high surface-to-volume ratio [57, 58]. However, the results disagreed. The conversion of 3-nitrostyrene at 0.5 h for 10-nm CTHs (Cu-Pd-3) was 75.6%, and the corresponding TOF value was 457.7 h^{-1} , slightly lower than the case of Cu-Pd-1. Figure S19 shows the time profiles for the three different catalysts.

Among the three reactions, that of the Cu-Pd-1 exhibited the highest conversion of 3-nitrostyrene (~90%), and that of the 50-nm Cu-Pd-2 exhibited the lowest conversion (less than 60%, as shown in Fig. S19). It is established that both the composition and structure of the nanocatalysts influence their catalytic properties. Our catalytic experiments were conducted with the same total amounts of Cu and Pd. A slight compositional difference was presented with Pd ratios of 95% for Cu-Pd-1, 93% for Cu-Pd-2, and 89% for Cu-Pd-3. The composition could function by modifying the electronic state of the primary component and binding properties of the species involved in the reaction [59]. Regarding the structure, the {111} and {110} facets of Cu-Pd-1 and Cu-Pd-3 contrast the {111} facet of Cu-Pd-2. In addition, Cu-Pd-1 exhibited a larger size and more obvious concavity than Cu-Pd-3. The catalysts' composition and structure both contributed to the differences in the catalytic results. Notably, the commercial Pd/C catalyst exhibited the highest activity (100% conversion of 3-nitrostyrene) and the corresponding highest TOF value (315.8 h^{-1}), together with 75.5% to 3-nitroethylbenzene at 0.5 h (Table 2). However, at 2 h, the 3-nitroethylbenzene in the product

Table 2 Catalytic results for hydrogenation of 3-nitrostyrene using various Cu-Pd alloy nanocrystals^a

catalyst	Time / h	Conversion / %	Selectivity / %		TOF ^e / h ⁻¹
					
10% Cu-Pd-1 ^b /C	0.5	77.7	>99.9	0	1205.4
	2	88.7	>99.9	0	344.0
10% Cu-Pd-2 ^c /C	0.5	35.9	>99.9	0	843.9
	2	45.9	>99.9	0	269.7
10% Cu-Pd-3 ^d /C	0.5	75.6	>99.9	0	457.7
	2	81.0	>99.9	0	122.6
10% Pd/C	0.5	100	75.5	24.5	315.8
	2	100	0	>99.9	78.9

^a Reaction conditions: catalyst (3 mg), substrate (0.3 mmol), dodecane (3 ml), H₂ (1 atm), reaction temperature (75 °C).

^b Cu-Pd-1, 48-nm CTHs.

^c Cu-Pd-2, 50-nm RTPs.

^d Cu-Pd-3, 10-nm CTHs.

^e TOF = [reacted mol substrate]/[(the number of surface metal atoms) × (reaction time)]. (see electronic supplementary material for details)

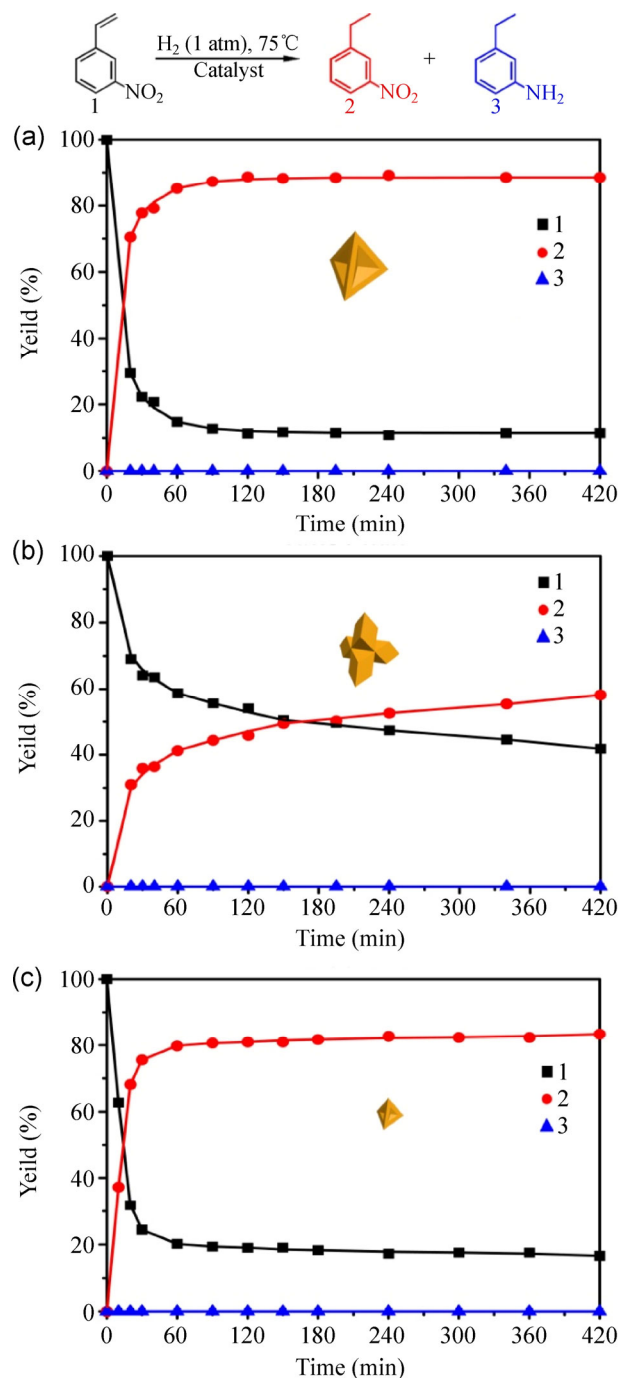


Figure 8 Time course of hydrogenation of 3-nitrostyrene with H₂ using (a) Cu-Pd-1, (b) Cu-Pd-2, and (c) Cu-Pd-3.

was hydrogenated completely to 3-aminoethylbenzene for Pd/C, whereas for the other three catalysts, there was interestingly almost no 3-aminoethylbenzene in the products after the three reactions reached thermodynamic equilibrium (Fig. 8). These results demonstrate that the three kinds of as-prepared Cu-Pd nanocrystals exhibited outstanding chemoselectivity

(>99.9%) toward the reduction of the C=C of 3-nitrostyrene and that they enabled the formation of 3-nitroethylbenzene without the further reduction of the nitro group to 3-aminoethylbenzene (Figs. 8(a)–8(c)).

4 Conclusion

We demonstrated a new strategy for the shape-controlled synthesis of Cu-Pd alloy nanocrystals by adding DA as a coordination ligand to achieve co-reduction. By varying the volume of DA in the system, we successfully synthesized Cu-Pd nanocrystals with different shapes, including THs, CTHs, RTPs, and TPs. Further research reveals that DA played an important role in the kinetic controlled synthesis. In addition to a coordination ligand, DA also served as a capping agent on {111} facets, prompting the corner-selective deposition and controlling the diffusion rate of the adatoms and thus leading to the formation of nanocrystals with different shapes. In addition, DA, as a Lewis base, enhanced the reduction power of the aldehyde group, which greatly influenced the reaction kinetics. Other reaction parameters, such as the temperature and the concentration of the reducing agent, were also ascertained to influence the morphologies of the nanocrystals. Three kinds of Cu-Pd nanocrystals (48-nm CTHs, 50-nm RTPs, and 10-nm CTHs) were evaluated as catalysts for the hydrogenation of 3-nitrostyrene and exhibited a high chemoselectivity to C=C instead of $-\text{NO}_2$. Among them, the 48-nm CTHs exhibited the highest conversion. We expect that this work will provide a novel strategy for the shape-controlled synthesis of bimetallic nanocrystals and will further our understanding of the co-reduction growth mechanism. Therefore, it promotes the application of these nanomaterials in catalysis, electrochemistry, and other areas.

Acknowledgements

This work was supported by Collaborative Innovation Center of Suzhou Nano Science and Technology, MOST of China (2014CB932700 and 2011CB921403), 2015SRG-HSC049, NSFC under Grant Nos. 21203173, 51371164, and 51132007, Strategic Priority Research Program B of the CAS under Grant No. XDB01020000,

and Fundamental Research Funds for the Central Universities (WK2340000050, WK3510000002 and WK2060190025).

Electronic Supplementary Material: Supplementary material (UV-vis extinction; FT-IR characterization; low-magnification TEM images; Enlarged HRTEM image on the edge of a typical CTH; XRD pattern; XPS spectra; ICP data; TEM image of Cu-Pd alloy nanocrystals obtained using the standard synthesis, except for the addition of TOA (170 μL) instead of DA; TEM images of Cu-Pd nanocrystals prepared using the standard procedure but without adding any DA or TOA; TEM image of Cu-Pd nanocrystals obtained using the standard synthesis, except for the addition of EDA (10%, 250 μL) instead of DA; TEM images of Cu-Pd bimetallic nanocrystals synthesized using the standard procedure, except for the addition of HCl or NaOH; TEM images of nanocrystals prepared using different amount of CuCl_2 ; TEM images of Cu-Pd nanocrystals prepared using the standard procedure but without the addition of PVP; higher magnification TEM images of Cu-Pd bimetallic nanocrystals shown in (a) Fig. 6(c) and (b) Fig. 6(d); the EDX spectrum of 10-nm CTHs; TEM images showing the effect of reaction temperature on the formation of Cu-Pd alloy nanocrystals; TEM images of products obtained at different times; conversion of 3-nitrostyrene for the three different nanocrystals; and calculation of the total number of atoms on the surface) is available in the online version of this article at <http://dx.doi.org/10.1007/s12274-015-0752-8>.

References

- [1] Rodriguez, J. A.; Goodman, D. W. The Nature of the Metal-Metal Bond in Bimetallic Surfaces. *Science* **1992**, 257, 897–903.
- [2] Chen, A.; Holt-Hindle, P. Platinum-Based Nanostructured Materials: Synthesis, Properties, and Applications. *Chem. Rev.* **2010**, 110, 3767–3804.
- [3] Habas, S. E.; Lee, H.; Radmilovic, V.; Somorjai, G. A.; Yang, P. D. Shaping binary metal nanocrystals through epitaxial seeded growth. *Nat. Mater.* **2007**, 6, 692–697.
- [4] Shen, S. L.; Zhuang, J.; Yang, Y.; Wang, X. Highly mono-disperse Cu- and Ag-based bimetallic nanocrystals for the efficient utilization of noble metals in catalysis. *Nanoscale*

- 2011, 3, 272–279.
- [5] Sugano, Y.; Shiraishi, Y.; Tsukamoto, D.; Ichikawa, S.; Tanaka, S.; Hirai, T. Supported Au–Cu Bimetallic Alloy Nanoparticles: An Aerobic Oxidation Catalyst with Regenerable Activity by Visible-Light Irradiation. *Angew. Chem. Int. Ed.* **2013**, 125, 5403–5407.
 - [6] Wang, D. S.; Li, Y. D. Bimetallic Nanocrystals: Liquid-Phase Synthesis and Catalytic Applications. *Adv. Mater.* **2011**, 23, 1044–1060.
 - [7] Son, S. U.; Jang, Y. J.; Park, J.; Na, H. B.; Park, H. M.; Yun, H. J.; Lee, J.; Hyeon, T. Designed Synthesis of Atom-Economical Pd/Ni Bimetallic Nanoparticle-Based Catalysts for Sonogashira Coupling Reactions. *J. Am. Chem. Soc.* **2004**, 126, 5026–5027.
 - [8] Peng, Z. M.; Yang, H. Synthesis and Oxygen Reduction Electrocatalytic Property of Pt-on-Pd Bimetallic Heteronanostructures. *J. Am. Chem. Soc.* **2009**, 131, 7542–7543.
 - [9] Dhital, R. N.; Kamonsatikul, C.; Somsook, E.; Bobuatong, K.; Ehara, M.; Karanjit, S.; Sakurai, H. Low-Temperature Carbon–Chlorine Bond Activation by Bimetallic Gold/Palladium Alloy Nanoclusters: An Application to Ullmann Coupling. *J. Am. Chem. Soc.* **2012**, 134, 20250–20253.
 - [10] Kang, Y. J.; Ye, X. C.; Chen, J.; Cai, Y.; Diaz, R. E.; Adzic, R. R.; Stach, E. A.; Murray, C. B. Design of Pt–Pd Binary Superlattices Exploiting Shape Effects and Synergistic Effects for Oxygen Reduction Reactions. *J. Am. Chem. Soc.* **2013**, 135, 42–45.
 - [11] Sneed, B. T.; Brodsky, C. N.; Kuo, C.-H.; Lamontagne, L. K.; Jiang, Y.; Wang, Y.; Tao, F.; Huang, W. X.; Tsung, C.-K. Nanoscale-Phase-Separated Pd–Rh Boxes Synthesized via Metal Migration: An Archetype for Studying Lattice Strain and Composition Effects in Electrocatalysis. *J. Am. Chem. Soc.* **2013**, 135, 14691–14700.
 - [12] Zhang, L.; Zhang, J. W.; Kuang, Q.; Xie, S. F.; Jiang, Z. Y.; Xie, Z. X.; Zheng, L. S. Cu²⁺-Assisted Synthesis of Hexoctahedral Au–Pd Alloy Nanocrystals with High-Index Facets. *J. Am. Chem. Soc.* **2011**, 133, 17114–17117.
 - [13] Kikhtyanin, O. V.; Rubanov, A. E.; Ayupov, A. B.; Echevsky, G. V. Hydroconversion of Sunflower oil on Pd/SAPO-31 Catalyst. *Fuel* **2010**, 89, 3085–3092.
 - [14] Nishihata, Y.; Mizuki, J.; Akao, T.; Tanaka, H.; Uenishi, M.; Kimura, M.; Okamoto, T.; Hamada, N. Self-Regeneration of a Pd-Perovskite Catalyst for Automotive Emissions Control. *Nature* **2002**, 418, 164–167.
 - [15] Kalita, B.; Deka, R. C. Reaction Intermediates of CO Oxidation on Gas Phase Pd₄ Clusters: A Density Functional Study. *J. Am. Chem. Soc.* **2009**, 131, 13252–13254.
 - [16] Adams, B. D.; Chen, A. C. The Role of Palladium in a Hydrogen Economy. *Mater. Today* **2011**, 14, 282–289.
 - [17] Yamauchi, M.; Abe, R.; Tsukuda, T.; Kato, K.; Takata, M. Highly Selective Ammonia Synthesis from Nitrate with Photocatalytically Generated Hydrogen on CuPd/TiO₂. *J. Am. Chem. Soc.* **2011**, 133, 1150–1152.
 - [18] Shao, M. H.; Shoemaker, K.; Peles, A.; Kaneko, K.; Protsailo, L. Pt Monolayer on Porous Pd–Cu Alloys as Oxygen Reduction Electrocatalysts. *J. Am. Chem. Soc.* **2010**, 132, 9253–9255.
 - [19] Zhang, F. X.; Miao, S.; Yang, Y. L.; Zhang, X.; Chen, J. X.; Guan, N. J. Size-Dependent Hydrogenation Selectivity of Nitrate on Pd–Cu/TiO₂ Catalysts. *J. Phys. Chem. C* **2008**, 112, 7665–7671.
 - [20] Mazumder, V.; Chi, M. F.; Mankin, M. N.; Liu, Y.; Metin, □.; Sun, D. H.; More, K. L.; Sun, S. H. A Facile Synthesis of MPd (M = Co, Cu) Nanoparticles and Their Catalysis for Formic Acid Oxidation. *Nano Lett.* **2012**, 12, 1102–1106.
 - [21] Moon, G. D.; Ko, S.; Min, Y.; Zeng, J.; Xia, Y. N.; Jeong, U. Chemical Transformations of Nanostructured Materials. *Nano Today* **2011**, 6, 186–203.
 - [22] Goris, B.; Polavarapu, L.; Bals, S.; Tendeloo, G. V.; Liz-Marzán, L. M. Monitoring Galvanic Replacement Through Three-Dimensional Morphological and Chemical Mapping. *Nano Lett.* **2014**, 14, 3220–3226.
 - [23] Zhang, H.; Jin, M. S.; Liu, H. Y.; Wang, J. G.; Kim, M. J.; Yang, D. R.; Xie, Z. X.; Liu, J. Y.; Xia, Y. N. Facile Synthesis of Pd–Pt Alloy Nanocages and Their Enhanced Performance for Preferential Oxidation of CO in Excess Hydrogen. *ACS Nano* **2011**, 5, 8212–8222.
 - [24] Mallin, M. P.; Murphy, C. J. Solution-Phase Synthesis of Sub-10 nm Au–Ag Alloy Nanoparticles. *Nano Lett.* **2002**, 2, 1235–1237.
 - [25] Zhang, Z. C.; Yang, Y.; Nosheen, F.; Wang, P. P.; Zhang, J. C.; Zhuang, J.; Wang, X. Fine Tuning of the Structure of Pt–Cu Alloy Nanocrystals by Glycine-Mediated Sequential Reduction Kinetics. *Small* **2013**, 9, 3063–3069.
 - [26] Xia, B. Y.; Wu, H. B.; Wang, X.; Lou, X. W. One-Pot Synthesis of Cubic PtCu₃ Nanocages with Enhanced Electrocatalytic Activity for the Methanol Oxidation Reaction. *J. Am. Chem. Soc.* **2012**, 134, 13934–13937.
 - [27] Fu, G. T.; Liu, Z. Y.; Chen, Y.; Lin, J.; Tang, Y. W.; Lu, T. H. Synthesis and Electrocatalytic Activity of Au@Pd Core–Shell Nanothorns for the Oxygen Reduction Reaction. *Nano Res.* **2014**, 7, 1205–1214.
 - [28] Zhang, Q.; Guo, X.; Liang, Z. X.; Zeng, J. H.; Yang, J.; Liao, S. J. Hybrid PdAg Alloy–Au nanorods: Controlled Growth, Optical Properties and Electrochemical Catalysis. *Nano Res.* **2013**, 6, 571–580.
 - [29] Mao, J. J.; Liu, Y. X.; Chen, Z.; Wang, D. S.; Li, Y. D. Bimetallic Pd–Cu Nanocrystals and Their Tunable Catalytic

- Properties. *Chem. Commun.* **2014**, 50, 4588–4591.
- [30] Nosheen, F.; Zhang, Z. C.; Xiang, G. L.; Xu, B.; Yang, Y.; Saleem, F.; Xu, X. B.; Zhang, J. C.; Wang, X. Three-dimensional Hierarchical Pt-Cu Superstructures. *Nano Res.* **2015**, 8, 832–838.
- [31] Park, K.-H.; Lee, Y. W.; Kang, S. W.; Han, S. W. A Facile One-Pot Synthesis and Enhanced Formic Acid Oxidation of Monodisperse Pd–Cu Nanocatalysts. *Chem. Asian J.* **2011**, 6, 1515–1519.
- [32] Zhang, L.; Hou, F.; Tan, Y. W. Shape-Tailoring of CuPd Nanocrystals for Enhancement of Electro-Catalytic Activity in Oxygen Reduction Reaction. *Chem. Commun.* **2012**, 48, 7152–7154.
- [33] Gao, Q.; Ju, Y. M.; An, D.; Gao, M. R.; Cui, C. H.; Liu, J. W.; Cong, H. P.; Yu, S. H. Shape-Controlled Synthesis of Monodisperse PdCu Nanocubes and Their Electrocatalytic Properties. *ChemSusChem* **2013**, 6, 1878–1882.
- [34] Mohl, M.; Dobo, D.; Kukovec, A.; Konya, Z.; Kordas, K.; Wei, J.; Vajtai, R.; Ajayan, P. M. Formation of CuPd and CuPt Bimetallic Nanotubes by Galvanic Replacement Reaction. *J. Phys. Chem. C* **2011**, 115, 9403–9409.
- [35] Gao, C. B.; Hu, Y. X.; Wang, M. S.; Chi, M. F.; Yin, Y. D. Fully Alloyed Ag/Au Nanospheres: Combining the Plasmonic Property of Ag with the Stability of Au. *J. Am. Chem. Soc.* **2014**, 136, 7474–7479.
- [36] Xia, X. H.; Xie, S. F.; Liu, M. C.; Peng, H.-C.; Lu, N.; Wang, J. G.; Kim, M. J.; Xia, Y. N. On the Role of Surface Diffusion in Determining the Shape or Morphology of Noble-Metal Nanocrystals. *Proc. Natl. Acad. Sci. U.S.A.* **2013**, 110, 6669–6673.
- [37] Liu, M. C.; Zheng, Y. Q.; Zhang, L.; Guo, L. J.; Xia, Y. N. Transformation of Pd Nanocubes into Octahedra with Controlled Sizes by Maneuvering the Rates of Etching and Regrowth. *J. Am. Chem. Soc.* **2013**, 135, 11752–11755.
- [38] Xie, S. F.; Zhang, H.; Lu, N.; Jin, M. S.; Wang, J. G.; Kim, M. J.; Xie, Z. X.; Xia, Y. N. Synthesis of Rhodium Concave Tetrahedrons by Collectively Manipulating the Reduction Kinetics, Facet-Selective Capping, and Surface Diffusion. *Nano Lett.* **2013**, 13, 6262–6268.
- [39] Inzelt, G. In *Encyclopedia of Electrochemistry*; Bard, A. J.; Stratmann, M.; Scholz, F.; Pickett, Ch., Eds.; Wiley-VCH: Weinheim, **2006**; Vol. 7, 42–43.
- [40] Inzelt, G. In *Encyclopedia of Electrochemistry*; Bard, A. J.; Stratmann, M.; Scholz, F.; Pickett, Ch., Eds.; Wiley-VCH: Weinheim, **2006**; Vol. 7, 511.
- [41] Denton, A. R.; Ashcroft, N. W. Vegard's Law. *Phys. Rev. A* **1991**, 43, 3161–3164.
- [42] Langille, M. R.; Personick, M. L.; Zhang, J.; Mirkin, C. A. Defining Rules for the Shape Evolution of Gold Nanoparticles. *J. Am. Chem. Soc.* **2012**, 134, 14542–14554.
- [43] Xia, X. H.; Zeng, J.; Oetjen, L. K.; Li, Q. G.; Xia, Y. N. Quantitative Analysis of the Role Played by Poly(vinylpyrrolidone) in Seed-Mediated Growth of Ag Nanocrystals. *J. Am. Chem. Soc.* **2012**, 134, 1793–1801.
- [44] Niesz, K.; Grass, M.; Somorjai, G. A. Precise Control of the Pt Nanoparticle Size by Seeded Growth Using EO₁₃PO₃₀EO₁₃ Triblock Copolymers as Protective Agents. *Nano Lett.* **2005**, 5, 2238–2240.
- [45] Zhang, D. Q.; Wang, R. R.; Wen, M. C.; Weng, D.; Cui, X.; Sun, J.; Li, H. X.; Lu, Y. F. Synthesis of Ultralong Copper Nanowires for High-Performance Transparent Electrodes. *J. Am. Chem. Soc.* **2012**, 134, 14283–14286.
- [46] Langille, M. R.; Zhang, J.; Mirkin, C. A. Plasmon-Mediated Synthesis of Heterometallic Nanorods and Icosahedra. *Angew. Chem. Int. Ed.* **2011**, 50, 3543–3547.
- [47] Ming, T.; Feng, W.; Tang, Q.; Wang, F.; Sun, L. D.; Wang, J. F.; Yan, C. H. Growth of Tetrahedral Gold Nanocrystals with High-Index Facets. *J. Am. Chem. Soc.* **2009**, 131, 16350–16351.
- [48] Casale, A.; Robertis, A. D.; Stefano, C. D.; Gianguzze, A.; Patanè, G.; Rigano, C.; Sammartano, S. Thermodynamic Parameters for the Formation of Glycine Complexes with Magnesium(II), Calcium(II), Lead(II), Manganese(II), Cobalt(II), Nickel(II), Zinc(II) and Cadmium(II) at Different Temperatures and Ionic Strengths, with Particular Reference to Natural Fluid Conditions. *Thermochim. Acta* **1995**, 255, 109–141.
- [49] Xiong, Y. J.; McLellan, J. M.; Chen, J. Y.; Yin, Y. D.; Li, Z. Y.; Xia, Y. N. Kinetically Controlled Synthesis of Triangular and Hexagonal Nanoplates of Palladium and Their SPR/SERS Properties. *J. Am. Chem. Soc.* **2005**, 127, 17118–17127.
- [50] Wang, C. Y.; Lin, C. K.; Zhang, L. H.; Quan, Z. W.; Sun, K.; Zhao, B.; Wang, F.; Porter, N.; Wang, Y. X.; Fang, J. Pt₃Co Concave Nanocubes: Synthesis, Formation Understanding, and Enhanced Catalytic Activity toward Hydrogenation of Styrene. *Chem. Eur. J.* **2014**, 20, 1753–1759.
- [51] Yin, A. X.; Min, X. Q.; Zhu, W.; Liu, W. C.; Zhang, Y. W.; Yan, C. H. Pt-Cu and Pt-Pd-Cu Concave Nanocubes with High-Index Facets and Superior Electrocatalytic Activity. *Chem. Eur. J.* **2012**, 18, 777–782.
- [52] Huang, X. Q.; Tang, S. H.; Zhang, H. H.; Zhou, Z. Y.; Zheng, N. F. Controlled Formation of Concave Tetrahedral/Trigonal Bipyramidal Palladium Nanocrystals. *J. Am. Chem. Soc.* **2009**, 131, 13916–13917.
- [53] Dai, Y.; Mu, X. L.; Tan, Y. M.; Lin, K. Q.; Yang, Z. L.; Zheng, N. F.; Fu, G. Carbon Monoxide-Assisted Synthesis of Single-Crystalline Pd Tetrapod Nanocrystals through Hydride Formation. *J. Am. Chem. Soc.* **2012**, 134, 7073–7080.

- [54] Chen, Y.-H.; Hung, H.-H.; Huang, M. H. Seed-Mediated Synthesis of Palladium Nanorods and Branched Nanocrystals and Their Use as Recyclable Suzuki Coupling Reaction Catalysts. *J. Am. Chem. Soc.* **2009**, *131*, 9114–9121.
- [55] Chen, M. S.; Kumar, D.; Yi, C.-W.; Goodman, D. W. The Promotional Effect of Gold in Catalysis by Palladium-Gold. *Science* **2005**, *310*, 291–293.
- [56] Narayanan R.; El-Sayed M. A. Shape-Dependent Catalytic Activity of Platinum Nanoparticles in Colloidal Solution. *Nano Lett.* **2004**, *4*, 1343–1348.
- [57] Shokouhimehr, M.; Kim, T.; Jun, S. W.; Shin, K.; Jang, Y. J.; Kim, B. H.; Kim, J.; Hyeon, T. Magnetically Separable Carbon Nanocomposite Catalysts for Efficient nitroarene Reduction and Suzuki Reactions. *Appl. Catal. A: Gen.* **2014**, *476*, 133–139.
- [58] Zeng, J.; Zhang, Q.; Chen, J. Y.; Xia, Y. N. A Comparison Study of the Catalytic Properties of Au-Based Nanocages, Nanoboxes, and Nanoparticles. *Nano Lett.* **2010**, *10*, 30–35.
- [59] Hong, J. W.; Kim, D.; Lee, Y. W.; Kim, M.; Kang, S. W.; Han, S. W. Atomic-Distribution-Dependent Electrocatalytic Activity of Au-Pd Bimetallic Nanocrystals. *Angew. Chem. Int. Ed.* **2011**, *123*, 9038–9042.

